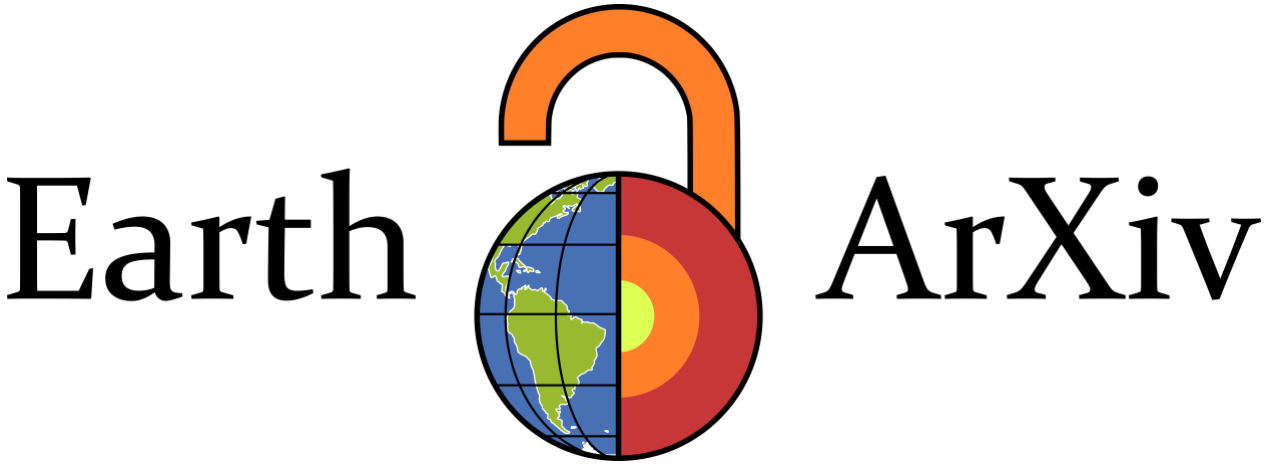

Quantification of Power Plant NO_x Emissions: A Reference for Diurnal and Seasonal Accuracy of TEMPO

Samuel J. Beaudry[1,2], Qindan Zhu[*2], and Ronald C. Cohen[*1,3]

[1]Department of Chemistry, University of California at Berkeley, Berkeley, CA, USA
[2]Smithsonian Astrophysical Observatory, Center for Astrophysics | Harvard & Smithsonian, Cambridge, MA, USA
[3]Department of Earth and Planetary Science, University of California at Berkeley, Berkeley, CA, USA

*Corresponding Authors: qindan.zhu@cfa.harvard.edu; rccohen@berkeley.edu

A reformatted edition of this manuscript has been submitted for publication in *Environmental Science & Technology*. Please note the manuscript has yet to be formally accepted for publication. Subsequent versions of this manuscript may have slightly different content. If accepted, the final version of this manuscript will be available via the 'Peer-reviewed Publication DOI' link on the right-hand side of this webpage.

Quantification of Power Plant NO_x Emissions: A Reference for Diurnal and Seasonal Accuracy of TEMPO

Samuel J. Beaudry[1,2], Qindan Zhu*[2], and Ronald C. Cohen*[1,3]

[1]Department of Chemistry, University of California at Berkeley, Berkeley, CA, USA
[2]Smithsonian Astrophysical Observatory, Center for Astrophysics | Harvard & Smithsonian, Cambridge, MA, USA
[3]Department of Earth and Planetary Science, University of California at Berkeley, Berkeley, CA, USA

*Email: qindan.zhu@cfa.harvard.edu; rccohen@berkeley.edu

Abstract

Satellite observations of NO_2 from geostationary orbit provide an opportunity to study daytime emissions with hourly temporal resolution. We used NO_2 column measurements from Tropospheric Emissions: Monitoring of Pollution (TEMPO) with a new fitting function, the rise-decay (RD) model, to derive NO_x emissions at 64 power plants in the continental United States. The RD model separately fits the rise of NO_2 line densities immediately downwind of the source and the decay of NO_x further downwind. This point source-specific function more reliably constrained emissions than the exponentially modified Gaussian (EMG) function, a typical method used to estimate NO_x emissions from space. The RD-derived emissions were compared with in situ emission measurements from the Continuous Emissions Monitoring Systems (CEMS). Average emissions were quantified within 50% accuracy at 27 of the power plants using TEMPO. Bias against CEMS was negatively correlated with emitter strength and was substantial at plants emitting less than 250 kg NO_2 per hour. The TEMPO-derived emissions reproduce the diurnal and seasonal patterns of CEMS reported emissions. These results demonstrate the utility of the rise-decay method for point source emitters and indicate the limits of TEMPO NO_2 for quantifying NO_x emissions.

Introduction

Constraining emissions of nitrogen oxides ($NO + NO_2 \equiv NO_x$) is one of the principal applications of space-based observations of column NO_2. Since NO_x is released in large quantities at industrial point sources and in urban areas, and has a lifetime on the order of hours, NO_2 vertical column densities (VCDs) are elevated near NO_x sources with sharp gradients between these sources and the background. For several decades, satellite instruments in low Earth orbit (LEO) have made observations of column NO_2 with increasing spatial resolution. Notably, the Ozone Monitoring Instrument (OMI),[1] launched in 2005, and the TROPOspheric Monitoring Instrument (TROPOMI), launched in 2017,[2] feature high enough spatial resolutions to enable a variety of approaches to derive NO_x emissions. With global coverage once per day at 13:30 local time, both OMI and TROPOMI have enabled studies of NO_x emissions from large industrial point sources[3–6] and in urban areas,[7–14] as well as been used to evaluate emission inventories.[15,16] The continental to near-global spatial coverage of these observations makes them especially powerful.

Tropospheric Emissions: Monitoring of Pollution (TEMPO), launched in 2023, observes trace gases from geostationary Earth orbit (GEO) over North America with a spatial resolution of 2×4.75 km^2 at the center of its field of regard (FOR).[17] Together with Geostationary Environment Monitoring Spectrometer (GEMS)

over East Asia[18] and Sentinel-4 over Europe,[19] TEMPO forms part of a geostationary constellation that makes sub-daily observations of NO_2 and other trace gases. TEMPO's hourly sampling provides repeated observations of NO_2 columns over NO_x source regions throughout daylight hours, extending beyond the early-afternoon sampling window of earlier LEO instruments. These observations could be used, for instance, to study hourly trends in NO_x emissions and lifetimes. The performance of the TEMPO NO_2 product was established by Szykman et al. (2025)[20] through validation with ground, airborne, and space-based observations. However, this validation does not necessarily establish TEMPO's ability to resolve hour-to-hour variations in emissions; this application requires evaluation against independent emission inventories.

Error in satellite-derived NO_x emissions arises from both the NO_2 VCDs themselves and the derivation method. Generally, emissions are proportional to the magnitude of the NO_2 column attributed to a source so that the uncertainty or bias in the column translates to the emission rate. For example, the emission rate at low wind speed can be approximated from the NO_2 column ratioed by the lifetime,[21] such that the column's relative error propagates directly to the emission. For tropospheric NO_2 VCDs, the sources of uncertainty can be separated into the fitting uncertainties associated with the slant column density (SCD), the uncertainty of the troposphere-stratosphere split, and the uncertainties in the air mass factor (AMF) used to convert from SCD to VCD.[22] For polluted scenes, the AMF uncertainties dominate the total uncertainty,[22] with low biases resulting from the use of modeled a priori NO_2 profiles at lower resolution than the satellite instrument.[23,24] Beaudry and Cohen (2026)[25] found that TEMPO tropospheric NO_2 VCDs increased by $\sim$25% near large NO_x sources using a signal-derived retrieval to adjust the lower-resolution prior of the TEMPO retrieval to match the observed pixel-to-pixel variation. A 25% low bias in peak NO_2 VCDs corresponds to similar biases in emissions: it directly propagates in steady state approaches where the emission rate is proportional to the column density, and indirectly affects emissions through the lifetime inferred from NO_2 spatial gradients. Accurately characterizing and correcting AMF-related biases is therefore necessary for robust satellite-derived NO_x emission estimates.

The method used to calculate emissions based on NO_2 VCDs introduces other sources of uncertainty. Approaches such as flux divergence[9,26–28] and the exponentially modified Gaussian (EMG)[7,8,13,29,30] assume a uniform wind field, with errors in the wind speed corresponding to errors in emissions. Flux divergence and other methods (such as the superposition model described by Lorente et al. (2019)[11]) also require a prescribed NO_x lifetime. Mols et al. (2026)[12] found a strong relationship between errors in the NO_x emission and lifetime, with a 50% underestimate in the lifetime corresponding to a 100% overestimate in emissions. Often, these lifetime values are assumed constant or taken from chemical transport models (CTMs), which may inaccurately represent the NO_x lifetime, especially due to their resolution.[31,32] The EMG approach simultaneously derives emissions and lifetime, but has high uncertainty at low wind speed and may not be appropriate for point sources which lack a spatial spread. Another source of uncertainty is the NO_x/NO_2 ratio needed to convert from the observed NO_2 to NO_x.[33]

Independent evaluation of satellite-derived NO_x emissions requires comparison with direct measurements. The continuous emissions monitoring systems (CEMS) make in situ measurements of NO_x emissions at most large power plants in the United States. Ground truth measurements from CEMS, typically only at a small subset of power plants, have been used in several studies of the accuracy of satellite-derived NO_x emissions.[3,5,6,34] Sun et al. (2025)[34] compared TEMPO emissions derived using the directional derivative method to CEMS values, finding that the TEMPO emissions were four times lower than the CEMS emissions and speculating that the low bias may be due to the uncertainty in the NO_x/NO_2 ratio. That study did not consider the chemical loss of NO_x within the 20×10 km windows around the power plants and investigated 14 of the largest power plants in the US.

In this study, we use TEMPO NO_2 to derive emissions at 64 US power plants by detecting individual plumes, converting 2D NO_2 columns to 1D line densities, and fitting these line densities to determine emissions and lifetime. We introduce a point source specific model, rise-decay, which treats the source as an impulse function rather than a Gaussian distribution as in the EMG method. The rise-decay and EMG methods are compared and assumptions of the rise-decay model are assessed using simulated column densities. The rise-decay method is then used to characterize NO_x emissions at 54 power plants in 2025 with at least 5 observations and known CEMS emission rates. Comparison against CEMS is used to determine the minimum emission rate that this method can quantify, and to assess how bias and uncertainty from the fitting procedure

and retrieval impact the derived emissions. Lastly, the diurnal and seasonal trends of the TEMPO-derived emissions are compared with those from CEMS.

Methods

Power Plant CEMS

In situ NO_x emission values were obtained from the Environmental Protection Agency's (EPA) Clean Air Markets Program (CAMP) data.[35] Unit level hourly data for 2025 were downloaded for all plants in the collection. Facility level data were obtained by summing each unit's emissions (in lbs NO_2) within each reporting hour to obtain hourly emission rates. Each unit of a facility may use CEMS or may estimate emissions with a formula (e.g. using the fuel flow rate and a NO_x emission factor).[36] To ensure that comparisons were with measured quantities, plant-hour pairs were only used if all operating units reported NO_x mass from CEMS. A unit's NO_x emission rate was flagged as CEMS if the NO_x mass measure indicator was "measured", or if both the NO_x rate measure indicator and heat input measure indicator were marked as "measured". Otherwise, the unit and facility were flagged as not using CEMS for that hour and excluded from comparisons with TEMPO-derived quantities. CEMS and TEMPO plume observations were matched by the same date and starting hour. For example, a TEMPO observation at 19:37 local standard time (LST) would be matched with the CEMS emissions reported for the 19:00 LST hour.

The latitude/longitude coordinates for the plant IDs in the CAMP data were obtained from `https://github.com/USEPA/camd-eia-crosswalk`. These were used to center the plume detection and fitting windows. These coordinates were also used to narrow analysis to plants that were isolated from urban areas and other power plants. The top ∼250 largest emitters in the CAMP data were considered. Plants were excluded if they were within 100 km of the center of one of the top 50 most populous Census Bureau Statistical Area (CBSA).[37,38] Plants were also excluded if they were within 30 km of another power plant with mean NO_x emissions in 2025 greater than 100 kg/hr (NO_2 equivalent weight). This removed plants located in rural areas but clustered together. Lastly, plants were manually confirmed to be visually isolated from developed areas. This process selected 67 plants to enter the plume detection procedure, with emissions successfully derived at 64 plants. (Table S3).

TEMPO NO_2

Version 4 (V04) of the TEMPO level 2 (L2) tropospheric NO_2 product was used for plume detection and quantification.[39] The operational TEMPO L2 NO_2 files were used to produce signal-derived retrieval (SDR) products as discussed in Beaudry and Cohen (2026).[25] Briefly, the SDR product differs from the operational product by redistributing the 25-km NO_2 profile from GEOS-CF within the boundary layer to be consistent with the observed NO_2 gradients. This leads to substantial increases in NO_2 VCD along the narrow point source plumes in this study. Only NO_2 VCDs meeting "update quality" in the SDR were used in the plume analysis; pixels failing this criteria were masked. The full conditions for this are given in Beaudry and Cohen (2026),[25] but the most relevant requirements are a main data quality flag of 0, maximum effective cloud fraction of 0.1, a maximum solar zenith angle of 70°, and a snow/ice fraction of zero. Most often, pixels are excluded due to high cloud fraction. Data from Jan - Dec 2025 were used.

Plume Detection

NO_2 plumes were detected at power plants in the CEMS inventory. Since TEMPO pixels are approximately 10 km^2, we treated facilities (including those with multiple units) as single point sources. For each plant, an 80-km window centered on the plant was cropped from the TEMPO-SDR level 2 tropospheric product. TEMPO pixels were matched with the lowest hybrid level wind field from the 3-km High Resolution Rapid Refresh (HRRR) reanalysis product.[40] The median wind vector within 20 km of the plant was used for the

wind direction and speed. The NO_2 tropospheric VCD fields were converted to ΔNO_2 fields by removing the background NO_2, estimated as the median NO_2 VCD in a 120° sector upwind of the source. For observations with fewer than 50 upwind pixels, the background was estimated as the 20th percentile of the NO_2 field.

The ΔNO_2 field was then used to recalculate the upwind background and determine the median absolute deviation (MAD) from the background at each pixel:

$$\text{MAD} = median\left(|\Delta NO_2 - \text{background}|\right) \quad (1)$$

Pixels with ΔNO_2 more than 3MAD above the background were flagged and grouped with adjacent flagged pixels. The largest group of flagged pixels was marked as a detected plume if it was at least 7 pixels large, within 10-km of the source location, aligned within 45° of the mean wind direction, and had more than 75% of detected pixels downwind of the site. These conditions reduced the number of false positives due to other sources and filtered out poor-quality observations resulting from missing or noisy data, large disagreement between the observed plume and modeled meteorology, and low wind speeds. The plume mask corresponding to the NO_2 in Figure 1(a) is shown in yellow in Figure 1(b).

Line Density Calculation

Line densities were computed using the NO_2 tropospheric VCD field and plume mask. For detected plumes, the NO_2 observation was cropped onto a 200-km window, and the plume mask was regenerated. Detected secondary plumes were used to remove pixels impacted by other sources in the window. The integration and fitting bounds of the line density were produced using the plume mask plus a 30-km upwind buffer, 50-km downwind buffer, and 15-km crosswind buffers (Figure 1(b)). The resulting box contained the NO_2 features to be fit while excluding other enhancements which may be in the region. The boxed pixels were rotated to align with the wind direction determined from HRRR (Figure 1(c)). To convert to line densities, the VCDs were sorted into 40 bins in the along-wind direction using the pixel centers. The total ΔNO_2 mass in each bin was divided by bin width to obtain line densities (black dots in Figure 1(d)). Pixels with missing data were assigned the average density of good quality pixels within the bin. Bins with less than 30% of the integration area observed by good pixels were masked. The resulting line densities were fit to obtain the emission rate and lifetime.

Line Density Fitting Functions

Rise-Decay

The rise-decay (RD) model assumes an isolated point source that can be approximated as a delta function. It treats separate parts of the plume as a piecewise function based on the distance from the source x (Equation 2). Upwind of the source, the line densities y have a constant background value B. To account for the TEMPO pixel size, which is 2.0×4.75 km^{-2} at the center of the field regard and becomes larger toward the edges, the upwind region is defined as more than 10 km upwind of the source location. At the source ($x = 0$), over 90% of the NO_x is emitted as NO.[4] This NO titrates the ozone near the stack, converting some of the NO to NO_2. This yields ozone-depleted conditions immediately downwind, with a high NO_x-NO_2 ratio.[33] As additional ozone is mixed into the plume, it is titrated to convert more of the NO to NO_2, represented as an exponential rise in the NO_2 line density with a mixing length scale x_m. We assume that in the ozone-depleted region of the plume, chemical and physical losses of NO_x can be neglected so that the total NO_x line density is constant and set by the NO_x emission rate and scalar advection rate w. The NO_2 line density increases to a maximum value y_{max} at a distance x_{max} downwind of the source. Since total NO_x is conserved up to this point, the emission rate E_{RD} is given by the product of y_{max}, wind speed w, and the NO_x-NO_2 ratio at that point (γ) (Equation 3). We assign the commonly used NO_x-NO_2 ratio of 1.32.[3,7]

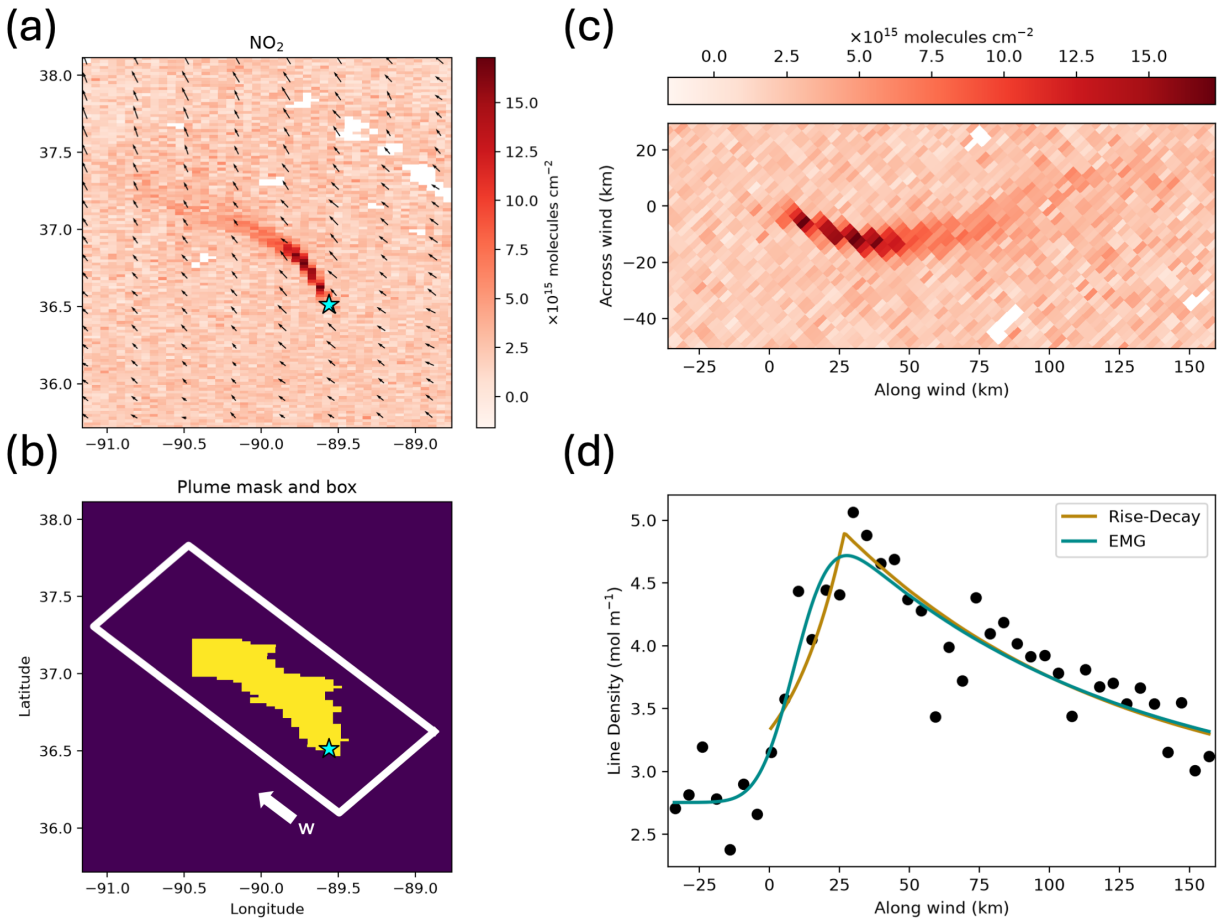

Figure 1: (a) TEMPO-SDR NO_2 tropospheric VCD on Scan 10 of 2025-11-06 (13:52 LST). Star marks the location of the New Madrid Power Plant. Black arrows show wind field from HRRR. Low quality pixels and pixels associated with secondary sources are masked white. (b) Plume shape identified from detection algorithm (yellow), average wind direction within 20 km of plant (white arrow), and box showing fitting domain along wind direction and integration bounds in the cross-wind direction. (c) NO_2 within fitting domain rotated to align with wind direction. (d) Line densities obtained by integrating NO_2 in (c) in the cross-wind dimension, with the corresponding rise-decay and EMG fits. For the rise-decay fit, only values downwind of the plant are shown but the function (Equation 2) was fit to all shown line densities.

$$y\left(x|x_{max}, y_{max}, x_m, x_d, B\right) = \begin{cases} B & \text{if } x < -10 \text{ km} \\ y_{max} exp\left[\frac{x - x_{max}}{x_m}\right] + B & \text{if } x \in [-10, x_{max}) \\ y_{max} exp\left[\frac{-(x - x_{max})}{x_d}\right] + B & \text{if } x \geq x_{max} \end{cases} \quad (2)$$

$$E_{RD} = y_{max} w \gamma \quad (3)$$

Starting at x_{max}, we assume that a stable NO_x-NO_2 ratio is reached and NO_x starts being removed from the plume (e.g. the reaction with OH to form HNO_3). This is observed as an exponential decay from y_{max} set by the e-folding parameter x_d, related to the NO_x lifetime by the wind speed w (Equation 4). An example of a RD fit is shown in Figure 1(d), where the function fits both the rise in NO_2 line density during the initial 30 km, followed by a sharp transition to an exponential decay profile.

$$\tau = \frac{x_d}{w} \quad (4)$$

The RD-derived emission is primarily dependent on x_{max}, y_{max}, and B. Unlike in other methods (e.g. exponentially modified Gaussian, flux divergence), this emission rate is not directly coupled to a derived or prescribed lifetime and its error derives principally from the error in y_{max}. The value of the mixing parameter x_m has no impact on the derived emissions. However, fitting the rise of NO_2 line densities enables the function to approximate the shape of the observed line densities and determine the location (x_{max}, y_{max}) to use for the emission derivation.

Exponentially Modified Gaussian

The exponentially modified Gaussian (EMG) is a popular fitting function for wind-aligned NO_2 line densities.[7,8,13,29,30] It is derived from the convolution of a Gaussian distribution (with mean μ and standard deviation σ) and an exponential decay function (with e-folding x_d). The Gaussian distribution describes the spread of sources in a given area and can also account for smoothing by the instrument. A higher value of σ corresponds to more dispersed sources. The exponential decay describes the loss of NO_x downwind from sources, especially due to reaction with OH.[29] The form of EMG used to derive emissions and lifetimes adds a scaling term related to the plume mass (A) and a background term (B) (Equation 5).

$$y\left(x|A, \mu, \sigma, x_d, B\right) = \frac{A}{2x_d} exp\left[\frac{1}{x_d}\left(\mu + \frac{\sigma^2}{2x_d} - x\right)\right] erfc\left[\frac{1}{\sqrt{2}\sigma}\left(\mu + \frac{\sigma^2}{x_d} - x\right)\right] + B \quad (5)$$

where $erfc$ is the complementary error function. As in the RD model, the observed e-folding x_d is related to the NO_x lifetime by the wind speed w (Equation 4). The emission rate E_{EMG} is derived from A and is inversely proportional to the lifetime and scaled by the NO_x-NO_2 ratio of the plume γ, which we again assume is 1.32 (Equation 6).

$$E_{EMG} = \frac{A}{\tau}\gamma \quad (6)$$

The EMG method has some distinct advantages, especially for characterizing plumes in cities. The Gaussian spread of the distribution can account for the dispersed NO_x sources in an urban area. The EMG also fits a lifetime derived from the observation instead of enforcing an a priori or modeled lifetime as in other methods.[9,28] This is important since, as in other methods, the emission value is strongly dependent on the lifetime (Equation 6). However, the EMG is poorly suited for strong point source emitters. A point source is better described as a delta function where pollutants are released at a single point instead of dispersed in space. Not only does this make the Gaussian distribution an inappropriate model for the source, but it challenges the assumption that chemical conditions are similar enough at all locations to derive a single NO_x lifetime. These challenges are apparent with the EMG fit in Figure 1(d), where the initially persistent

Table 1: Requirements to use RD fit in comparison with CEMS

Parameter	Condition
w	≥ 2 m s^{-1}
R^2	≥ 0.3
τ	(0.5 hr, 10 hr)
$\frac{y_{max}}{B}$	≥ 0.3

plume is fit as a somewhat dispersed source in order to simultaneously capture the clear exponential decay further downwind. Another weakness of the EMG is the difficulty distinguishing x_d and σ, especially at low wind speeds. Since the EMG-derived emission is sensitive to all of the fit parameters in Equation 5, the uncertainties in these parameters translate to large uncertainty in the emission rate. For these reasons, the RD model is a more appropriate fitting function to derive the NO_x emissions of power plants and other point sources.

Function Optimization

The RD function was fit to all line densities at detected plumes. The optimal parameters were determined using non-linear least squares via the "optimize.curve_fit" function in the SciPy Python library with 10,000 maximum function evaluations. Initial parameters and fitting constraints for the RD and EMG functions are provided in Tables S1 and S2 in the Supplement. Before comparison with CEMS measurements, RD-derived emission estimates were retained only if they satisfied the quality control criteria in Table 1. A moderate to high wind speed was required since advection translates the plant's emission rate to the observed line density (Equation 3) and relates e-folding and lifetime (Equation 4). The R^2 condition removes very poor fits but allows moderately successful fits since the derived emission depends mostly on the maximum line density. Urban NO_x lifetimes range from 1 to 6 hours,[41] but power plants of the size in this study may have downwind lifetimes of up to 10 hours.[4] The allowed lifetime range reflects this while removing unrealistic fits. Lastly, requiring the maximum line density to be at least 30% the background value removes fits where the emission signal may be indistinguishable from the uncertainty in satellite measured NO_2 columns.[22]

After filtering, there were 4,408 TEMPO-derived emission values across 64 power plants in 2025, including at 54 plants where at least five TEMPO-derived emissions were matched with non-zero CEMS-reported emissions.

Results and discussion

Performance of EMG and RD Functions

Both the RD and EMG functions were fitted to all detected plumes. Figure 2 demonstrates how poorly constrained parameters make EMG an inappropriate model for narrow point source plumes. One EMG function was fit with a procedure allowing σ to vary between 0.3 and 50 km ("wide", shown in the lighter color) while another EMG function was fit with σ constrained between 0.3 and 10 km ("narrow", shown in the darker color). In both cases, the e-folding scale x_d was allowed to vary from 1-100 km. While both EMG curves look similar, the emission estimate from the "wide" EMG (with $\sigma = 15$ km) is over 10 times greater than the estimate from the "narrow" EMG (with $\sigma = 10$ km). Representing the observed line density profile as a highly dispersed plume requires an unrealistically short lifetime of 0.1 hours. In this case, the optimization procedure selected the minimum allowed value of 1 km for x_d. Restricting σ in the "narrow" case reduces the fit R^2 from 0.87 to 0.83, but produces emissions more comparable in magnitude to those from the RD fit and the CEMS ground truth.

The substantial differences between derived emissions in Figure 2 illustrate major drawbacks of the EMG method which are avoided with the RD method. Since EMG-derived emissions are coupled with lifetimes

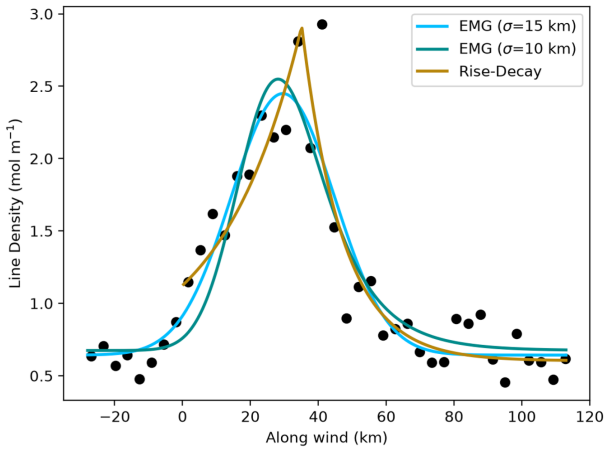

	Emission [kg/hr]	Lifetime [hr]	Fit R^2	x_d [km]	σ [km]	A [kmol]
EMG (Wide σ allowed)	40,000	0.1	0.87	1	15	69
EMG (Narrow σ required)	2,900	1.4	0.83	12	10	64
Rise-Decay	1,280	1.3	0.87	12		
CEMS	1,885					

Figure 2: Left: Line densities with EMG and RD fits for plume at New Madrid Power Plant on Scan 10 of 2025-03-13. Two EMG functions are shown: in the lighter blue color with $\sigma = 15$ km and in the darker green color with $\sigma = 10$ km. The RD fit downwind of the plant is shown in light brown. Right: table of fit results for the three functions, including in situ CEMS emissions for UTC hour 19:00 at New Madrid. Emission, lifetime, and parameter values are expressed to the precision indicated by the parameter fitting uncertainties. The fit R^2 for RD applies to both the upwind and downwind parts of the fit (Equation 2), not just the downwind portion shown on the left plot.

(Equation 6), errors in the derived lifetime directly propagate into the derived emissions even though the plume mass A is well constrained. In contrast, the emission rate from RD is not directly coupled to the derived lifetime and depends primarily on the maximum line density y_{max} (Equation 3), which is well constrained by the plume in Figure 2. The downwind e-folding x_d is also derived without being convolved with other parameters, whereas in the EMG approach it is coupled to σ. Forcing EMG spread to resemble a point source ($0.3 \leq \sigma \leq 10$ km) produces fits with correlated emissions between the EMG and RD methods ($r = 0.89$) and generally larger EMG-derived emissions compared to RD-derived emissions (Figure S1(a)), but R^2 tends to be higher for the RD fits (Figure S1(c)) and EMG more frequently fits long lifetimes (>5 hours) (Figure S1(d)). Moreover, fit σ values almost always reach the upper bound of 10 km (Figure S1(b)), indicating that EMG is poorly optimized for these point source plumes.

To test the assumptions of the RD method independently of satellite retrieval error, the plume detection and fitting method was applied to column densities simulated by Krol et al. (2024)[4] using the MicroHH large eddy simulation (LES) (Supplement). The simulation represents a point source emitting 2085 kg h^{-1}, which is comparable to the largest emitters in the CEMS inventory. While no loss of total NO_x is assumed in the RD model, the NO_x line density decays by $\sim 12\%$ before reaching the point of maximum NO_2 line density fit by RD (Figure S2(b)). The modeled NO_x/NO_2 ratio at this point is also 1.48 while the assumed value is 1.32 (Figure S2(c)). Together, these impacts suggest that the RD-derived emission should be biased low $\sim$25%. However, the RD-derived emission using the MicroHH columns is only biased low $\sim$14%. When the MicroHH columns are gridded to TEMPO resolution, the magnitude of this bias increases (Figure S3), but introducing noise produces a sample distribution that is on average biased low $\sim$14% (Figure S4). Using the same model output, Meier et al.[33] found that the NO_x/NO_2 ratio depends on emitter strength and distance downwind from the source. The magnitude of the low bias resulting from these assumptions likely depends on the emitter size.

Evaluation of TEMPO-Derived Emissions

The RD-derived TEMPO emissions were compared with in situ CEMS emissions at 54 sites where at least 5 successful RD fits were matched with non-zero CEMS reported emissions. The sites feature a range of median emissions, from less than 100 kg/hr (NO_2 equivalent) at the lowest emitters to over 2000 kg/hr at

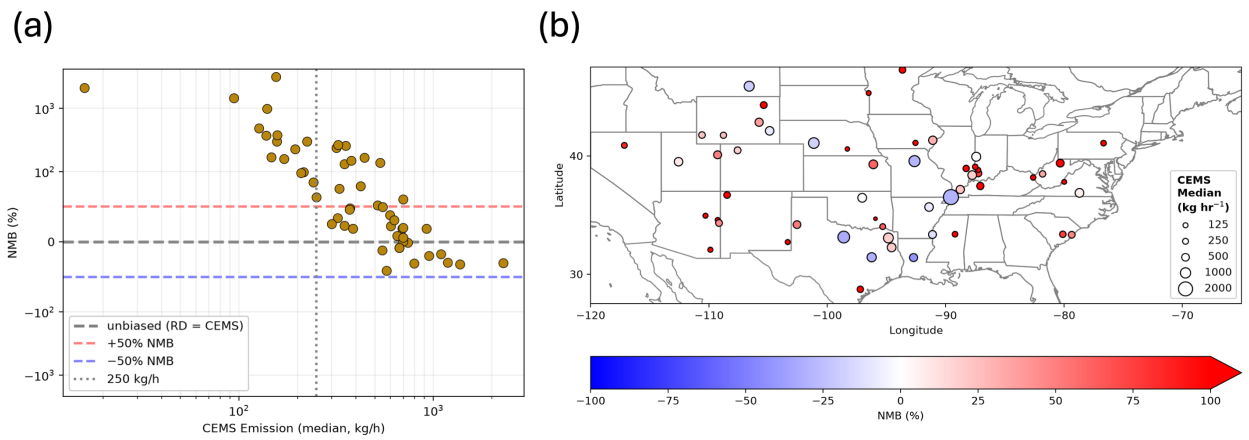

Figure 3: (a) Normalized mean bias (NMB) vs. median CEMS emission for RD-fit plumes at 54 CEMS-reporting plants with at least 5 coincident TEMPO and non-zero CEMS measurements. (b) Locations of the 54 power plants represented in (a), with plant locations colored by NMB and sized according to the median CEMS emission rate for the matched observations.

the highest emitters. Figure 3(a) shows the relationship between the normalized mean bias (NMB) of the TEMPO estimates and the CEMS emissions at each site. NMB decreases systematically with the source strength. For all plants with median emissions below 250 kg/hr, NMB is greater than 100% and worsens with decreasing emission rate. This threshold indicates the minimum emission rate that can be reliably quantified by TEMPO using the RD method. With one exception, all plants with median emissions above 600 kg/hr have NMB within ±50 %. Nevertheless, the negative relationship between NMB and the true emission rate persists. For the four plants with median emissions greater than 1000 kg/hr, NMB is persistently negative and is about −30% at the highest emitters.

Negative bias at the highest emitters, as seen in the plants above ∼800 kg/hr in Figure 3, is consistent with Sun et al. (2025).[34] Using the directional derivative approach, their NO_x emission rates derived from TEMPO V03 NO_2 were generally four times lower than emissions from CEMS at 14 power plants with an average emission rate of ∼ 750 kg/hr. Our approach yields emissions that are within ±50% of the CEMS values at these larger emitters. In addition to using a different emission-inference method, our analysis uses the V04 NO_2 product adjusted with the signal-derived retrieval (SDR). The SDR accounts for the gradient smoothing caused by the use of GEOS-CF profiles at 25-km spatial resolution and increases VCDs by up to 20-30%,[25] but other sources of systematic bias in the AMF calculation persist. For example, the absolute magnitude of the modeled NO_2 column is biased low if the emission inventories are inaccurate or, model meteorology places plumes in the wrong model pixels, or the NO_x lifetime in the model is not correct. The evaluation of the RD method with the MicroHH simulated columns suggests that half or more of the observed −30% bias results from assumptions in the RD method. The remaining negative bias at the highest emitters results from systematic errors in the retrieval.

The high bias at low emitters has multiple causes and is impacted by retrieval uncertainties. First, the VCDs associated with these sources are relatively small and more easily confounded by neighboring sources, such as other point sources or populated areas. While the plume detection method and site selection are intended to avoid this, any failures will disproportionately affect low emitters since their signal is already low. Second, as the emission rate drops below 250 kg/hr, the magnitude of the expected VCDs (and line densities) becomes comparable to the instrument noise. For example, a 100 kg/hr source with a 3 m/s wind field would have a maximum NO_2 line density of 0.15 mol/m (Equation 3). For a 10-km wide plume, this corresponds to an average NO_2 VCD below 10^{15} molecules/cm^2, which is comparable to the slant column fitting uncertainty and below the precision requirement for the TEMPO mission.[42] Since this floor is potentially reached by 100 kg/hr, it explains that NMB grows linearly with further decreases in the true emission rate.

To probe the impacts of random retrieval uncertainty, a bootstrapping experiment was performed using a

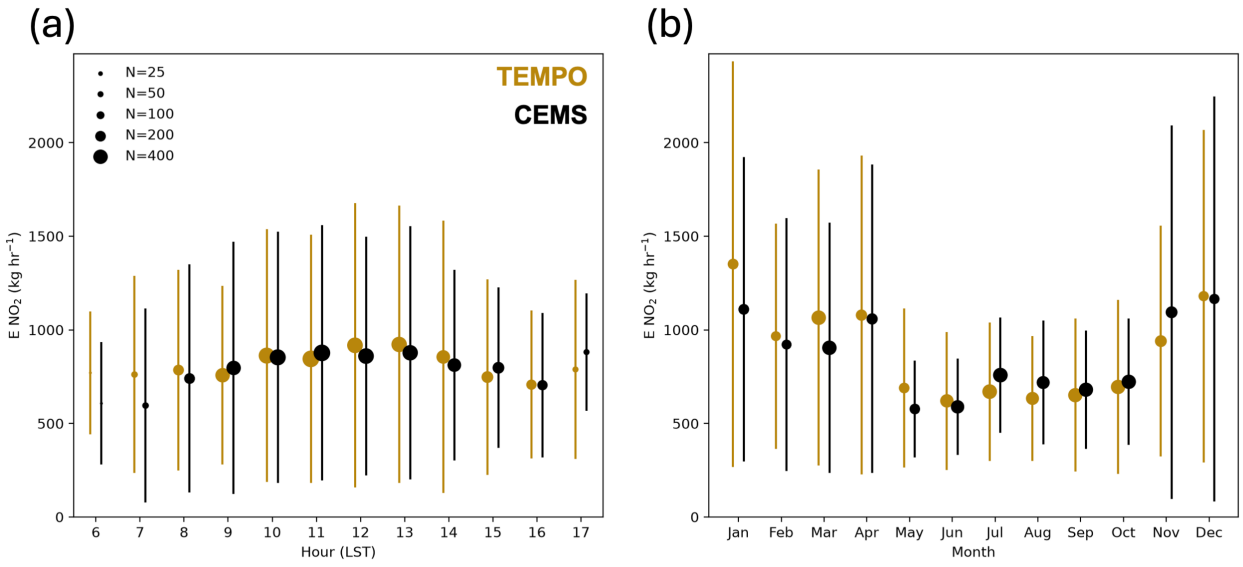

Figure 4: (a) Mean RD-derived TEMPO (light brown) and CEMS (black) emissions for observations with CEMS emissions >250 kg/hr. Emissions are grouped by local hour. (b) Same as (a), but grouped by month. For both plots, circles show mean and error bars show standard deviation of averaged emissions. Circle size corresponds to number of observations.

clear sky plume observation with a true emission rate of 1121 kg/hr and an RD-derived emission rate of 500 kg/hr (Supplement). Two uncertainty estimates were obtained: one using the reported slant column uncertainties at each pixel, and one using the larger of 1×10^{15} molecules/cm^2 or 30% relative uncertainty at each pixel. The standard deviations of derived emissions were 62 kg/hr and 95 kg/hr using the slant column and asserted uncertainties, respectively. These uncertainties are not large enough to explain the two times underestimation of this plume's true emissions (Figure S5), which is attributable to structured uncertainties in the retrieval and the assumptions of the derivation method. However, averaging the derived emissions at a source with consistent emissions can reduce the influence of these random uncertainties to obtain a more reliable estimate than from individual observations. This method's reliance on wind speed and direction introduces additional sources of error, including uncertainties in modeled wind speeds and misalignment between the wind direction and the plume. In one instance, adjusting the plume rotation to better follow the NO_2 gradient decreased the RD-derived emission by over 100 kg/hr (∼10%) (Figure S6). In other cases, realigning the plume increased the emission rate or did not significantly affect it, suggesting that this is a source of random uncertainty but does not introduce a systematic bias.

Accuracy of TEMPO Variations in Time

Though the uncertainty of individual observations and missing data (e.g. due to cloud cover) make it difficult to evaluate the hour-to-hour emission rate of a single plume, the hourly trend of mean TEMPO emissions agrees well with CEMS measurements. Figure 4(a) shows the hourly trend in mean TEMPO-derived and CEMS emissions among observations with CEMS emissions >250 kg/hr. The CEMS emission rates remain nearly constant during daylight hours, making them a useful benchmark to assess the accuracy of hourly trends observed by TEMPO. The mean TEMPO emission rates derived using RD are also similar from hour to hour, with all rates between 640 kg/hr and 930 kg/hr. These mean TEMPO values are comparable to those from CEMS, since the average includes plants that are both systematically overestimated and underestimated by TEMPO. While the TEMPO mean is within 10% of the CEMS mean from 8-18 LST, it is more than 20% larger at 7 LST. Ghahremanloo et al. (2025)[43] found that TEMPO total NO_2 was biased high compared to Pandora reference measurements primarily during early morning hours, with smaller differences in the late

afternoon/evening. This could be consistent with the morning overestimation in Figure 4(a), though there are fewer observations at this time to compare with CEMS. Systematic bias between TEMPO and CEMS emerges at individual plants (consistent with Figure 3), but the hour-to-hour pattern remains similar (Figure S7). These results show the utility of TEMPO V04 NO_2 to determine emissions at most hours during the day, with no large change in bias from hour to hour.

The power plant emissions exhibit a pronounced seasonal trend which is captured in the TEMPO-derived emissions. Figure 4(b) shows that CEMS emissions are highest in the winter months, with a smaller peak in summer and the lowest values in fall and spring. This seasonal cycle is consistent with fossil fuel electricity production in the U.S., which is highest during summer months and has a secondary peak during winter months.[44] Although electric demand is highest in the summer, the NO_x emission rate per unit of heat input is higher in winter (Figure S8), leading to the trend seen in Figure 4(b). While this trend is also seen in the TEMPO derived emissions, the TEMPO mean tends to be higher than CEMS in winter (e.g. $\sim$ 20% higher in January and March) and lower than CEMS in summer (e.g. $\sim$ 10% lower in July and August). This suggests a seasonal effect on the derived emissions independent from emitter strength, since Figure 3 would otherwise indicate that the TEMPO values would underestimate CEMS more during periods of high emission. Winter NO_2 VCDs tend to be higher than summer VCDs due to the longer NO_2 lifetime against photolysis in winter.[15] Future studies could investigate how this seasonality of the NO_2 lifetime impacts satellite-derived emissions (e.g. through the assumptions of the RD method), such as by comparing against modeled lifetimes.

Conclusions

We defined a point source-specific model, rise-decay (RD), to evaluate the limits and errors associated with TEMPO-derived NO_x emissions. The RD method produces more reliable derived emissions for point sources compared to the EMG method, which has poorly constrained parameters and emissions coupled to the derived lifetime. Using TEMPO VCDs, the RD method can quantify emissions above 250 kg/hr, with normalized mean bias improving to $\pm$50% at emitters with a median rate above 600 kg/hr. This demonstrates that this method is approaching the $\sim$100 kg/hr limit expected by the TEMPO instrument uncertainty, with the potential for further improvements (e.g. improved representation of the wind field). Normalized mean bias decreases with CEMS-reported emission rate and remains negative for the largest emitters (>1000 kg/hr), indicating systematic underestimation that depends on source strength. In contrast, mean TEMPO and CEMS values both showed minimal hourly trend, suggesting that bias in TEMPO-derived emissions is not time of day dependent. The seasonal cycle of the CEMS emissions is also captured by TEMPO. These findings provide a framework for understanding the applicability of TEMPO for measuring NO_x emissions with different types of emitters and emission strengths. The limits of quantification and errors described here should inform future studies of satellite-derived emissions, especially for sources which lack a ground truth to verify against.

Data Availability

TEMPO L2 V04 NO_2 data sets are available from Liu (2026).[39] Code for the TEMPO signal-derived retrieval (SDR) is available at `https://github.com/sbeaudry18/Signal_Derived_Retrieval`. HRRR data is available at `https://registry.opendata.aws/noaa-hrrr-pds`. CEMS emissions are available from the Environmental Protection Agency's Clean Air Markets Program Data portal `https://campd.epa.gov/`. The locations of these plants were obtained from `https://github.com/USEPA/camd-eia-crosswalk` and matched with the CEMS data using the shared ORIS ID. The MicroHH outputs are available from Krol (2023).[45] The version of plume detection and fitting code used in this study is available at Beaudry and Zhu,[46] including the NO_2 VCDs and line densities used to derive emissions.

Acknowledgments

The authors acknowledge support from TEMPO project Grant SV3-83019. Q.Z. acknowledges support from the Smithsonian Astrophysical Observatory Independent Research and Development (IR&D) program. The supplemental text "Simulated Plume Analysis", supplemental figures, and elements of the discussion used MicroHH simulation outputs provided by Maarten Krol (https://doi.org/10.5281/zenodo.10053684). Computing resources were provided by the Smithsonian Institution High Performance Cluster (SI/HPC, https://doi.org/10.25572/SIHPC) and by the Savio computational cluster resource provided by the Berkeley Research Computing program at the University of California, Berkeley (supported by the UC Berkeley Chancellor, Vice Chancellor for Research, and Chief Information Officer).

Supporting information

The following files are available free of charge.

- supplement.pdf: Contains supplemental texts "Simulated Plume Analysis" and "TEMPO Bootstrapping Experiment", supplemental Tables S1-S2, and supplemental Figures S1-S8
- supplemental_table_S3.csv: Power plant locations and number of fits

References

(1) Levelt, P.; van den Oord, G.; Dobber, M.; Malkki, A.; Visser, H.; Vries, J. d.; Stammes, P.; Lundell, J.; Saari, H. The ozone monitoring instrument. *IEEE Transactions on Geoscience and Remote Sensing* **2006**, *44*, 1093–1101, DOI: 10.1109/TGRS.2006.872333.

(2) Veefkind, J. P. et al. TROPOMI on the ESA Sentinel-5 Precursor: A GMES mission for global observations of the atmospheric composition for climate, air quality and ozone layer applications. *Remote Sensing of Environment* **2012**, *120*, 70–83, DOI: 10.1016/j.rse.2011.09.027.

(3) De Foy, B.; Lu, Z.; Streets, D. G.; Lamsal, L. N.; Duncan, B. N. Estimates of power plant NOx emissions and lifetimes from OMI NO2 satellite retrievals. *Atmospheric Environment* **2015**, *116*, 1–11, DOI: 10.1016/j.atmosenv.2015.05.056.

(4) Krol, M.; van Stratum, B.; Anglou, I.; Boersma, K. F. Evaluating NO_x stack plume emissions using a high-resolution atmospheric chemistry model and satellite-derived NO_2 columns. *Atmospheric Chemistry and Physics* **2024**, *24*, 8243–8262, DOI: 10.5194/acp-24-8243-2024.

(5) Kuhlmann, G.; Koene, E. F. M.; Schooling, C. N.; Palmer, P. I.; López, Ò. C.; Guevara, M. Temporal variability of NO_x emissions from power plants: a comparison of satellite- and inventory-based estimates. *Atmospheric Chemistry and Physics* **2026**, *26*, 4405–4421, DOI: 10.5194/acp-26-4405-2026.

(6) Tang, T.; Cheng, T.; Zhu, H.; Ye, X.; Fan, D.; Li, X.; Tong, H. Quantifying instantaneous nitrogen oxides emissions from power plants based on space observations. *Science of The Total Environment* **2024**, *938*, 173479, DOI: 10.1016/j.scitotenv.2024.173479.

(7) Beirle, S.; Boersma, K. F.; Platt, U.; Lawrence, M. G.; Wagner, T. Megacity Emissions and Lifetimes of Nitrogen Oxides Probed from Space. *Science* **2011**, *333*, 1737–1739, DOI: 10.1126/science.1207824.

(8) Beirle, S.; Wagner, T. A new method for estimating megacity NO_x emissions and lifetimes from satellite observations. *Atmospheric Measurement Techniques* **2024**, *17*, 3439–3453, DOI: 10.5194/amt-17-3439-2024.

(9) De Foy, B.; Schauer, J. J. An improved understanding of NOx emissions in South Asian megacities using TROPOMI NO_2 retrievals. *Environmental Research Letters* **2022**, *17*, 024006, DOI: 10.1088/1748-9326/ac48b4.

(10) Liu, F.; Beirle, S.; Zhang, Q.; Dörner, S.; He, K.; Wagner, T. NO_{<i>x</i>} lifetimes and emissions of cities and power plants in polluted background estimated by satellite observations. *Atmospheric Chemistry and Physics* **2016**, *16*, 5283–5298, DOI: 10.5194/acp-16-5283-2016.

(11) Lorente, A.; Boersma, K. F.; Eskes, H. J.; Veefkind, J. P.; van Geffen, J. H. G. M.; de Zeeuw, M. B.; Denier van der Gon, H. a. C.; Beirle, S.; Krol, M. C. Quantification of nitrogen oxides emissions from build-up of pollution over Paris with TROPOMI. *Scientific Reports* **2019**, *9*, 20033, DOI: 10.1038/s41598-019-56428-5.

(12) Mols, A.; Boersma, K. F.; Denier van der Gon, H.; Krol, M. An improved Bayesian inversion to estimate daily NO_x emissions of Paris from TROPOMI NO_2 observations between 2018–2023. *Atmospheric Chemistry and Physics* **2026**, *26*, 1497–1513, DOI: 10.5194/acp-26-1497-2026.

(13) Pommier, M. Estimations of NO $_x$ emissions, NO $_2$ lifetime and their temporal variation over three British urbanised regions in 2019 using TROPOMI NO $_2$ observations. *Environmental Science: Atmospheres* **2023**, *3*, 408–421, DOI: 10.1039/D2EA00086E.

(14) Sun, K. Derivation of Emissions From Satellite-Observed Column Amounts and Its Application to TROPOMI NO2 and CO Observations. *Geophysical Research Letters* **2022**, *49*, e2022GL101102, DOI: 10.1029/2022GL101102.

(15) Goldberg, D. L.; Tao, M.; Kerr, G. H.; Ma, S.; Tong, D. Q.; Fiore, A. M.; Dickens, A. F.; Adelman, Z. E.; Anenberg, S. C. Evaluating the spatial patterns of U.S. urban NOx emissions using TROPOMI NO2. *Remote Sensing of Environment* **2024**, *300*, 113917, DOI: 10.1016/j.rse.2023.113917.

(16) Lu, Z.; Streets, D. G.; De Foy, B.; Lamsal, L. N.; Duncan, B. N.; Xing, J. Emissions of nitrogen oxides from US urban areas: estimation from Ozone Monitoring Instrument retrievals for 2005–2014. *Atmospheric Chemistry and Physics* **2015**, *15*, 10367–10383, DOI: 10.5194/acp-15-10367-2015.

(17) Zoogman, P. et al. Tropospheric emissions: Monitoring of pollution (TEMPO). *Journal of Quantitative Spectroscopy and Radiative Transfer* **2017**, *186*, 17–39, DOI: 10.1016/j.jqsrt.2016.05.008.

(18) Kim, J. et al. New Era of Air Quality Monitoring from Space: Geostationary Environment Monitoring Spectrometer (GEMS). *Bulletin of the American Meteorological Society* **2020**, *101*, E1–E22, DOI: 10.1175/BAMS-D-18-0013.1.

(19) Courrèges-Lacoste, G. B.; Sallusti, M.; Bulsa, G.; Bagnasco, G.; Veihelmann, B.; Riedl, S.; Smith, D. J.; Maurer, R. In 2017; Vol. 10423, pp 62–70, DOI: 10.1117/12.2282158.

(20) Szykman, J.; Pierce, R. B.; Henderson, B.; Judd, L. Validation and Quality Assessment of the TEMPO Level-2 Trace Gas Products. **2025**.

(21) Liu, F.; Tao, Z.; Beirle, S.; Joiner, J.; Yoshida, Y.; Smith, S. J.; Knowland, K. E.; Wagner, T. A new method for inferring city emissions and lifetimes of nitrogen oxides from high-resolution nitrogen dioxide observations: a model study. *Atmospheric Chemistry and Physics* **2022**, *22*, 1333–1349, DOI: 10.5194/acp-22-1333-2022.

(22) Boersma, K. F.; Eskes, H. J.; Brinksma, E. J. Error analysis for tropospheric NO2 retrieval from space. *Journal of Geophysical Research: Atmospheres* **2004**, *109*, DOI: 10.1029/2003JD003962.

(23) Zhao, X.; Griffin, D.; Fioletov, V.; McLinden, C.; Cede, A.; Tiefengraber, M.; Müller, M.; Bognar, K.; Strong, K.; Boersma, F.; Eskes, H.; Davies, J.; Ogyu, A.; Lee, S. C. Assessment of the quality of TROPOMI high-spatial-resolution NO_2 data products in the Greater Toronto Area. *Atmospheric Measurement Techniques* **2020**, *13*, 2131–2159, DOI: 10.5194/amt-13-2131-2020.

(24) Liu, S. et al. An improved TROPOMI tropospheric NO_2 research product over Europe. *Atmospheric Measurement Techniques* **2021**, *14*, 7297–7327, DOI: 10.5194/amt-14-7297-2021.

(25) Beaudry, S. J.; Cohen, R. C. A Signal-Derived Retrieval Reduces Bias in TEMPO NO_2. *Journal of Geophysical Research: Atmospheres* **2026**, *131*, e2025JD045606, DOI: 10.1029/2025JD045606.

(26) Beirle, S.; Borger, C.; Dörner, S.; Li, A.; Hu, Z.; Liu, F.; Wang, Y.; Wagner, T. Pinpointing nitrogen oxide emissions from space. *Science Advances* **2019**, *5*, eaax9800, DOI: 10.1126/sciadv.aax9800.

(27) Xu, T.; Zhang, C.; Xue, J.; Hu, Q.; Xing, C.; Liu, C. Estimating Hourly Nitrogen Oxide Emissions over East Asia from Geostationary Satellite Measurements. *Environmental Science & Technology Letters* **2023**, acs.estlett.3c00467, DOI: 10.1021/acs.estlett.3c00467.

(28) Cifuentes, F.; Eskes, H.; Dammers, E.; Bryan, C.; Boersma, F. Accurate space-based NO_x emission estimates with the flux divergence approach require fine-scale model information on local oxidation chemistry and profile shapes. *Geoscientific Model Development* **2025**, *18*, 621–649, DOI: 10.5194/gmd-18-621-2025.

(29) Valin, L. C.; Russell, A. R.; Cohen, R. C. Variations of OH radical in an urban plume inferred from NO2 column measurements. *Geophysical Research Letters* **2013**, *40*, 1856–1860, DOI: 10.1002/grl.50267.

(30) Jin, X.; Zhu, Q.; Cohen, R. C. Direct estimates of biomass burning NO_x emissions and lifetimes using daily observations from TROPOMI. *Atmospheric Chemistry and Physics* **2021**, *21*, 15569–15587, DOI: 10.5194/acp-21-15569-2021.

(31) Valin, L. C.; Russell, A. R.; Hudman, R. C.; Cohen, R. C. Effects of model resolution on the interpretation of satellite NO_2 observations. *Atmospheric Chemistry and Physics* **2011**, *11*, 11647–11655, DOI: 10.5194/acp-11-11647-2011.

(32) Li, C.; Martin, R. V.; Cohen, R. C.; Bindle, L.; Zhang, D.; Chatterjee, D.; Weng, H.; Lin, J. Variable effects of spatial resolution on modeling of nitrogen oxides. *Atmospheric Chemistry and Physics* **2023**, *23*, 3031–3049, DOI: 10.5194/acp-23-3031-2023.

(33) Meier, S.; Koene, E. F. M.; Krol, M.; Brunner, D.; Damm, A.; Kuhlmann, G. A lightweight NO_2-to-NO_x conversion model for quantifying NO_x emissions of point sources from NO_2 satellite observations. *Atmospheric Chemistry and Physics* **2024**, *24*, 7667–7686, DOI: 10.5194/acp-24-7667-2024.

(34) Sun, K.; Saju, J. A.; Nowlan, C. R.; González Abad, G.; Liu, X. Hourly Nitrogen Oxides Emissions Estimated From TEMPO and Comparison With Facility-Level Monitoring Data. *Journal of Geophysical Research: Atmospheres* **2025**, *130*, e2025JD044565, DOI: 10.1029/2025JD044565.

(35) United States Environmental Protection Agency (EPA) Power Sector Data [Dataset], 2026.

(36) United States Environmental Protection Agency (EPA) Power Sector Emissions Data Guide, 2022.

(37) United States Census Bureau Metropolitan and Micropolitan Statistical Area Population Totals and Components of Change: 2020-2025 [Dataset], 2026.

(38) U.S. Department of Commerce, U.S. Census Bureau, Geography Division TIGER/Line Shapefile, Current, Nation, U.S., Core Based Statistical Areas, 2025.

(39) Liu, X. TEMPO NO2 tropospheric and stratospheric columns V04 (PROVISIONAL) [Dataset], 2026, DOI: 10.5067/IS-40E/TEMPO/NO2_L2.004.

(40) Dowell, D. C. et al. The High-Resolution Rapid Refresh (HRRR): An Hourly Updating Convection-Allowing Forecast Model. Part I: Motivation and System Description. *Weather and Forecasting* **2022**, *37*, 1371–1395, DOI: 10.1175/WAF-D-21-0151.1.

(41) Laughner, J. L.; Cohen, R. C. Direct observation of changing NOx lifetime in North American cities. *Science* **2019**, *366*, 723–727, DOI: 10.1126/science.aax6832.

(42) Nowlan, C. R.; Abad, G. G.; Liu, X.; Wang, H.; Chance, K. TEMPO Nitrogen Dioxide Retrieval Algorithm Theoretical Basis Document. **2025**, DOI: 10.5067/8YMVQJZZP6S2.

(43) Ghahremanloo, M.; Nowlan, C.; González Abad, G.; Garraffo, C.; Liu, X.; Wang, H.; Henderson, B.; Baumann, E.; Valin, L.; Geddes, J. A.; Zhao, X. Comprehensive Analysis of Bias in TEMPO NO2 Column Densities Through Pandora Observations. *Journal of Geophysical Research: Atmospheres* **2025**, *130*, e2025JD044150, DOI: 10.1029/2025JD044150.

(44) U.S. Energy Information Administration (eia) Monthly Energy Review: Table 7.2a Electricity Net Generation: Total (All Sectors), 2026.

(45) Maarten Krol Code, input, output, and analysis software of the CoCO2 paper, submitted to Atmospheric Chemistry and Physics (Version 1.0) [Computer software], 2023, DOI: 10.5281/zenodo.10053684.

(46) Beaudry, S.; Zhu, Q. Code and output data for Quantification of Power Plant NOx Emissions: A Reference for Diurnal and Seasonal Accuracy of TEMPO [Computer software], 2026, DOI: 10.5281/zenodo.22822485.

Supplement to "Quantification of Power Plant NO_x emissions: A Reference for Diurnal and Seasonal Accuracy of TEMPO"

Samuel J. Beaudry[1,2], Qindan Zhu*[2], and Ronald C. Cohen*[1,3]

[1]Department of Chemistry, University of California at Berkeley, Berkeley, CA, USA
[2]Smithsonian Astrophysical Observatory, Center for Astrophysics | Harvard & Smithsonian, Cambridge, MA, USA
[3]Department of Earth and Planetary Science, University of California at Berkeley, Berkeley, CA, USA

*Email: qindan.zhu@cfa.harvard.edu; rccohen@berkeley.edu

Supplemental Text

Simulated Plume Analysis

To test the performance and assumptions of the RD method without the impact of observation error, we fit column densities produced by Krol et al. (2024)[1] using the MicroHH large eddy simulation (LES). Krol (2023)[2] modeled plumes with 100-m horizontal resolution at 4 global power plants, all with higher emission rates than any sites in the CEMS inventory. The Jänschwalde plant had a modeled emission rate of 12.59 mol/s (2085 kg/hr), which is comparable in magnitude to the largest CEMS emitters (see Figure 3). The modeled May 22, 2028 Jänschwalde plume is shown in Figure S2(a), where eddies and other structures are apparent downwind from the source. NO and NO_2 line densities were produced as in Figure 1. Figure S2(b) shows that total NO_x has decayed by ∼12.5% at 9-km, which suggests that assumption of constant NO_x in the rise section of the RD model may lead to systematically low values. Figure S2(c) shows the RD fit of the NO_2 line densities and the modeled NO_x/NO_2 ratio. Since the MicroHH plume has only 10-km of upwind line densities, line densities from -30 km to -10 km were inserted using the mean value from -10 to 0 km so that the RD background could be fit. At the maximum line density used to derive emissions, the modeled NO_x/NO_2 ratio is 1.48 while the assumed value is 1.32. This introduces another ∼11% underestimation of the true NO_x emission rate. This would suggest that the RD-derived emission should be biased 20-25% low, though it is actually fit as 1790 kg/hr (-14% compared to the true value.)

The role of the TEMPO instrument resolution and noise was also assessed. Figure S3(a) shows the MicroHH Jänschwalde plume gridded to TEMPO resolution. The line densities (Figure S3(d)) corresponding to the gridded data are noisier than those using the 100-m resolution data (Figure S2(c)), and the RD-derived emission value decreases from 1790 kg/hr to 1481 kg/hr (-29%). To test the robustness of this value, 1000 sampled observations of the plume were generated by bootstrapping the gridded plume (Figure S4). For each pixel, the sampled VCD was drawn from a normal distribution centered on the true value with standard deviation set by the larger of 1×10^{15} molecules cm^{-2} or 30% relative uncertainty. The distribution of sampled emissions is shown on the right of Figure S4. The center of the RD-derived emissions distribution, 1800 kg/hr, is similar to the value obtained using the MicroHH columns at 100-m resolution, though the standard deviation is substantial at over 300 kg/hr. This suggests that the assumptions in the RD method have a larger impact on the observed negative bias than TEMPO's spatial resolution or instrument noise.

TEMPO Bootstrapping Experiment

The role of uncertainty in the TEMPO NO_2 column densities was tested with a bootstrapping experiment. A clear-sky observation of a plume at the Gerald Gentleman, NE plant (Figure S5) was used to generate sample column maps using two uncertainty estimates. The first was the reported uncertainty in the TEMPO NO_2 product, which only corresponds to the slant column fitting uncertainties.[3] The absolute uncertainty was scaled by the signal-derived retrieval (SDR) adjustment to maintain the same relative uncertainty. Since the true uncertainty tends to be dominated by air mass factor (AMF) errors at more polluted pixels, by more than 20%,[4] a second "asserted" uncertainty estimate took the larger of 1×10^{15} molecules cm^{-2}, the TEMPO mission precision requirement,[3] or 30% relative uncertainty. Each pixel was treated independently to draw sample column densities from a Gaussian distribution centered on the measured VCD and with standard deviation set by the uncertainty. 1000 sampled VCD maps were produced this way and fit with the RD method.

The right panel of Figure S5 shows that the uncorrelated pixel uncertainties lead to a 62 kg/hr and 95 kg/hr spread in the derived emissions (for the SCD uncertainty and asserted uncertainty, respectively). This accounts for some of the spread in RD-derived emissions at single power plants (e.g. in Figure 4 and Figure S7). The distribution of derived emissions is much narrower than in the bootstrapped samples of the MicroHH plume, since the 30% relative uncertainty corresponds to a larger absolute uncertainty with the much higher VCDs in that example. The RD-fit emission for this plume is about twice as small as the CEMS emission, which remains far outside the sampled distribution. This suggests that uncertainty in the TEMPO NO_2 product cannot explain the negative bias observed at large emitters among the CEMS facilities. However, this analysis does not consider systematic biases that may have structure in space, such due to the gas profile or surface reflectance. Our use of the SDR product should account for up to 20-30% of the bias introduced by the low resolution gas profile.[5]

Supplemental Tables

Table S1: RD Parameter Initial Guesses and Bounds

Parameter	Initial Guess	Bounds
x_m	10 km	(1 km, 100 km)
x_d	30 km	(1 km, 100 km)
x_{max}	x_i[argmax(y_i)]	(0 km, max(x_i))
y_{max}	max(y_i) − B	(1 km, 10^4 km)
B	mean(y_i) where $\mathrm{x}_i < -10$ km	(-max(y_i), +max(y_i))

Table S2: EMG Parameter Initial Guesses and Bounds

Parameter	Initial Guess	Bounds
A	Integral of line densities	(0, 100×Initial Guess)
μ	0 km	In x domain
σ	5 km	(0.5 km, 50 km) "Wide" or (0.3 km, 10 km) "Narrow"
x_d	20 km	(1 km, 100 km)
B	median(y_i)	(-max(y_i), +max(y_i))

The caption for Table S3, uploaded separately, is given below.

- Table S3: Power Plant Locations and Number of Fits

References

(1) Krol, M.; van Stratum, B.; Anglou, I.; Boersma, K. F. Evaluating NO_x stack plume emissions using a high-resolution atmospheric chemistry model and satellite-derived NO_2 columns. *Atmospheric Chemistry and Physics* **2024**, *24*, 8243–8262.

(2) Maarten Krol Code, input, output, and analysis software of the CoCO2 paper, submitted to Atmospheric Chemistry and Physics (Version 1.0) [Computer software], 2023.

(3) Nowlan, C. R.; Abad, G. G.; Liu, X.; Wang, H.; Chance, K. TEMPO Nitrogen Dioxide Retrieval Algorithm Theoretical Basis Document. **2025**, DOI: 10.5067/8YMVQJZZP6S2.

(4) Boersma, K. F.; Eskes, H. J.; Brinksma, E. J. Error analysis for tropospheric NO2 retrieval from space. *Journal of Geophysical Research: Atmospheres* **2004**, *109*, DOI: 10.1029/2003JD003962.

(5) Beaudry, S. J.; Cohen, R. C. A Signal-Derived Retrieval Reduces Bias in TEMPO NO_2. *Journal of Geophysical Research: Atmospheres* **2026**, *131*, e2025JD045606.

Supplemental Figures

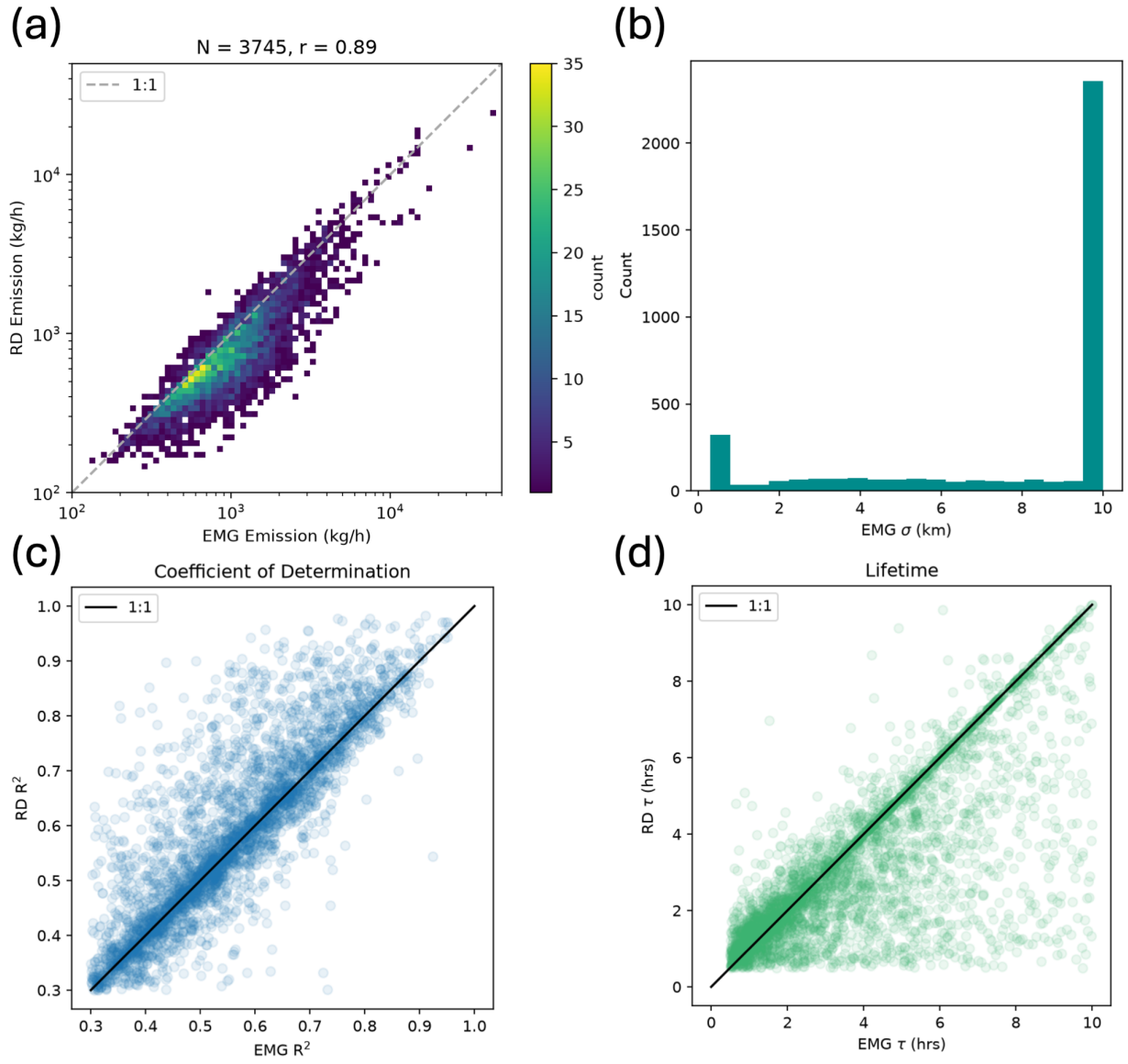

Figure S1: RD and EMG fit results meeting the criteria in Table 1 of the main text and constraining the EMG spread parameter between 0.3 and 10 km. (a) Scatter density plot of RD vs. EMG emissions. (b) Histogram of the fit EMG σ parameter. (c) Scatter plot comparing coefficient of determination between RD and EMG fits. (d) Scatter plot comparing lifetime between RD and EMG fits.

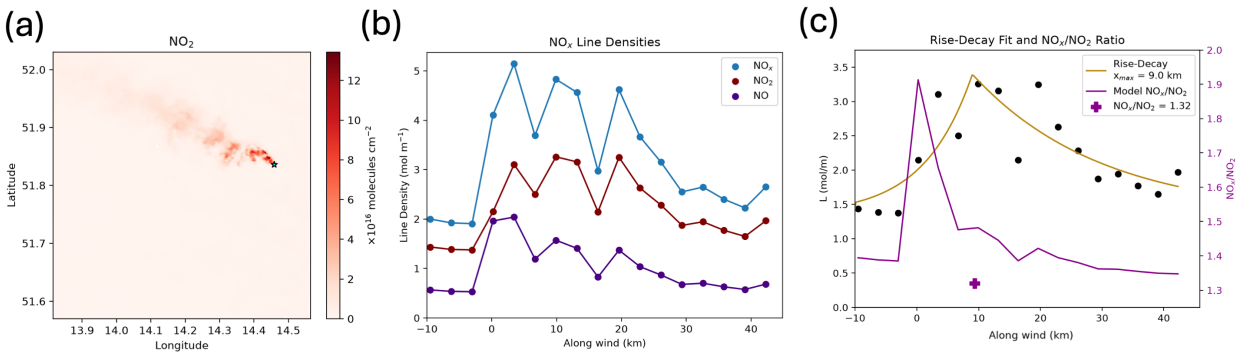

Figure S2: (a) NO_2 VCDs for the 100-m simulation of the Jänschwalde plume on May 22, 2018. (b) NO, NO_2, and NO_x line densities produced by integrating in the cross wind direction. (c) NO_2 line densities (black dots) with RD-fit in light brown and the NO_x/NO_2 ratio in magenta. The magenta plus is located at the RD-fit of x_{max} used to derive emissions and at the assumed NO_x/NO_2 ratio of 1.32.

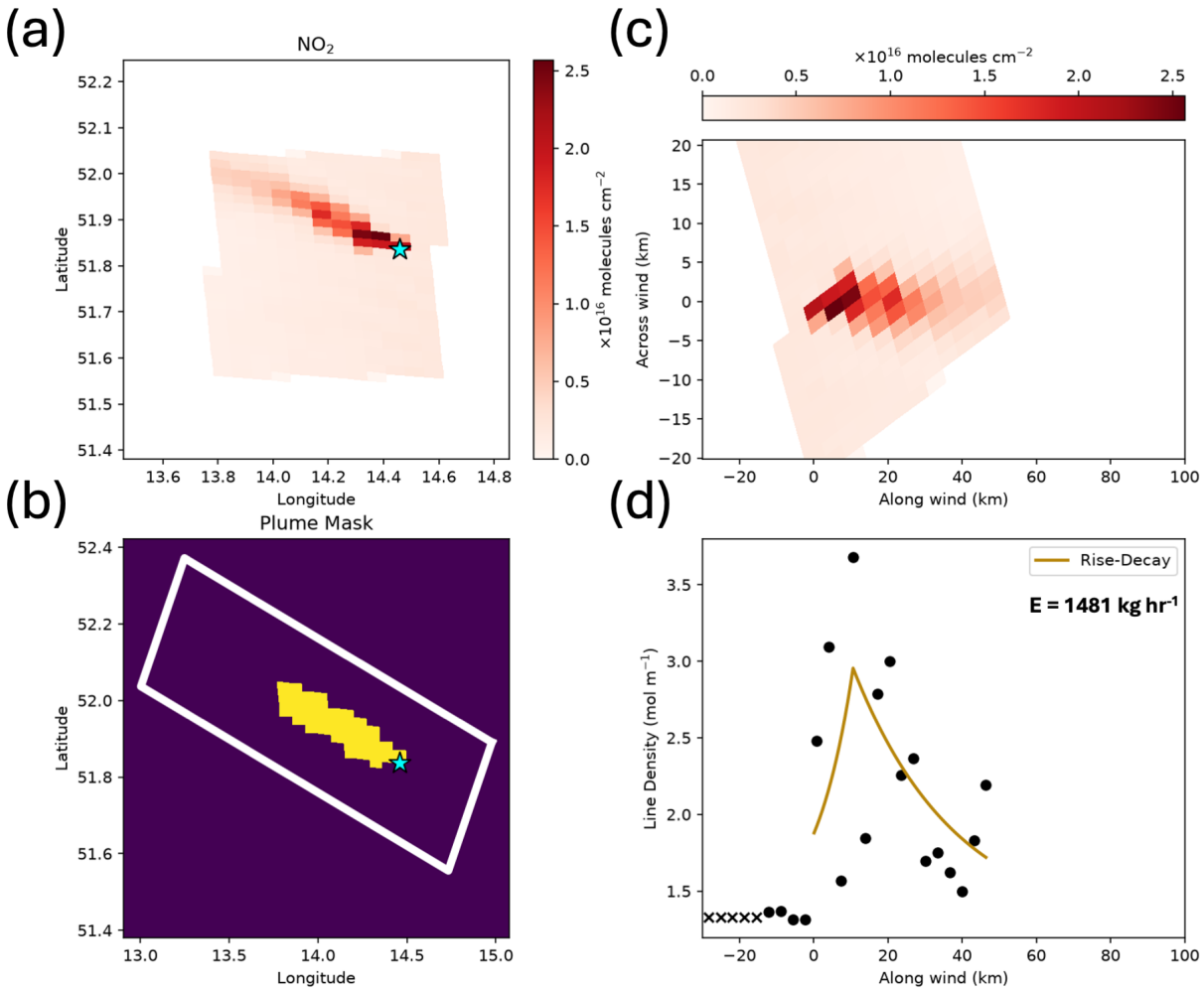

Figure S3: Similar to Figure 1 in main text, using MicroHH NO_2 column densities gridded to TEMPO resolution for the May 22, 2018 Jänschwalde plume. (a) NO_2 VCDs (b) Plume mask generated from detection algorithm. (c) Rotated NO_2 field within integration bounds. (d) Integrated line densities (circles) with RD fit. Line densities marked by x take the mean value of the other upwind line densities to enable fitting of the background.

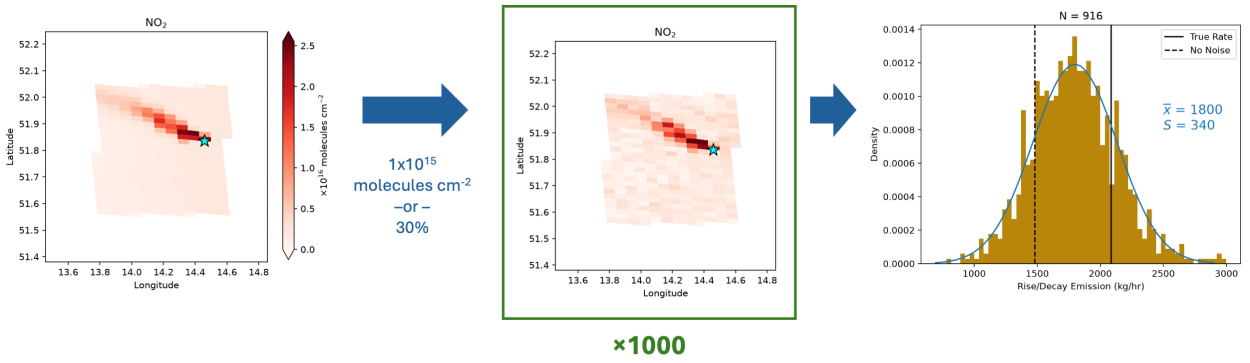

Figure S4: Bootstrapping scheme and results for MicroHH Jänschwalde plume. Left: MicroHH NO_2 VCDs gridded to TEMPO resolution are shown on the left. Middle: one of the 1,000 bootstrapped samples produced by drawing on normal distributions centered on each pixel's value with standard deviation set by the larger of 1×10^{15} molecules cm^{-2} or 30%. Right: the distribution of RD-derived emissions for fits meeting the requirements in Table 1. Mean and standard deviation of the distribution are shown in blue. The emission rate using the noise-free VCDs is shown by the dashed line, and the true emission rate is shown by the solid line.

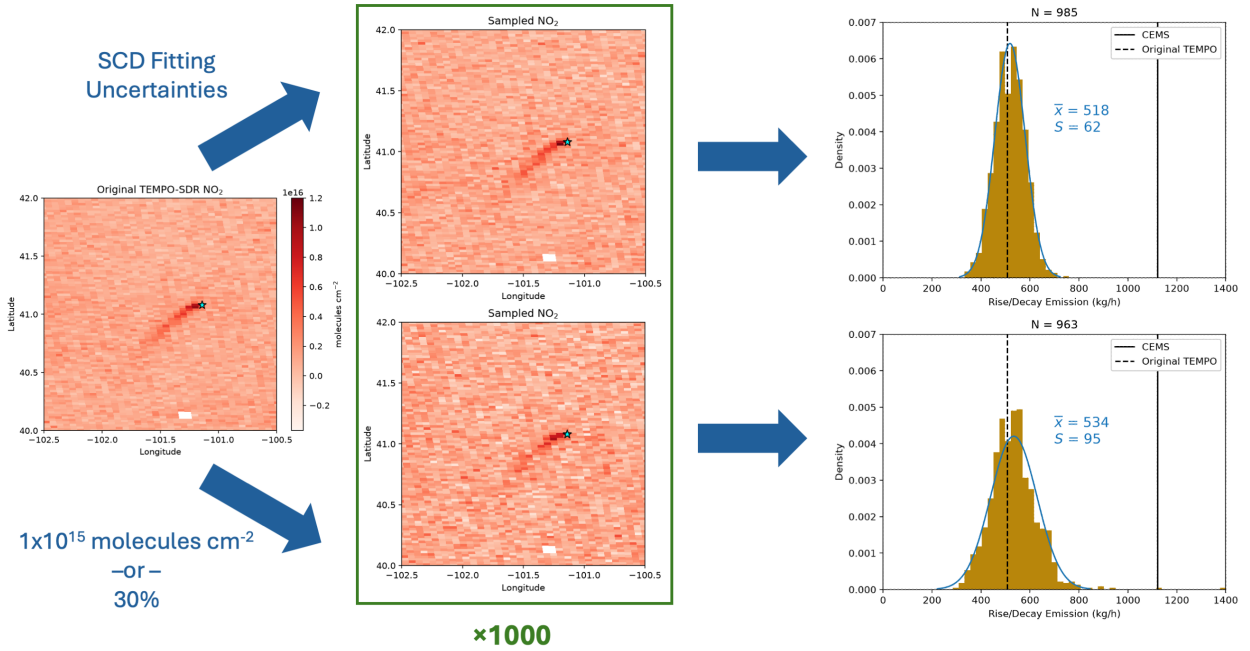

Figure S5: Bootstrapping scheme and results using a TEMPO observation of the Gerald Gentleman plant at 22:42:37 UTC on August 26, 2023. The left plot shows the TEMPO-SDR NO_2 tropospheric column densities. The middle plot shows column densities drawn from distributions centered on the true values and with uncertainty taken from, on the top, SCD fitting uncertainties and, on the bottom, the larger of $1{\times}10^{15}$ molecules cm^{-1} or 30% of the observed tropospheric VCD. This was repeated 1000 times and placed through the plume fitting procedure to obtain distributions of RD-derived emissions, shown on the right. Only RD fits meeting the quality criteria in Table 1 are included. The CEMS emission value is shown with the solid line; the derivation using the original TEMPO-SDR VCDs is shown in the dashed line. The mean and standard deviation of fit normal distributions are shown to the right of each distribution.

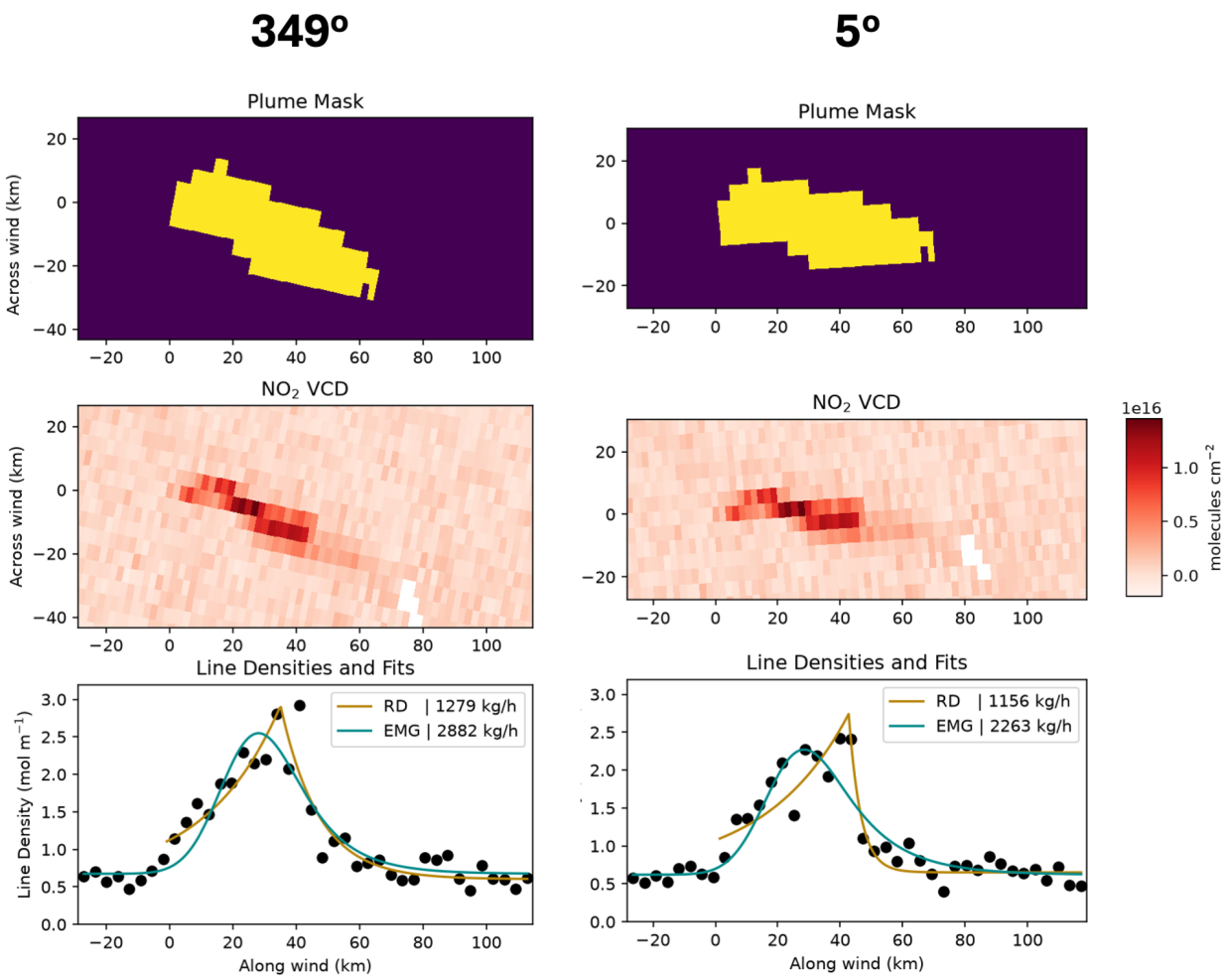

Figure S6: Plume fitting process for Scan 10 of 2025-03-13 at New Madrid Power Plant using two wind directions for rotation. Left column: 349^o, the median wind vector from HRRR within 20 km of the plant (as described in the methods). Right column: 5^o, manually selected to better align with the NO_2 gradient. Directions follow meteorological convention (0^o = vector pointing North, 90^o = vector pointing East, etc.) Top row: wind-aligned plume mask used to set integration bounds. Middle row: wind-aligned NO_2 VCDs within integration window. Bottom row: NO_2 line densities and fit results using EMG and RD functions. The same wind speed (2.53 m s^{-1}) is used to derive emission rates in each example.

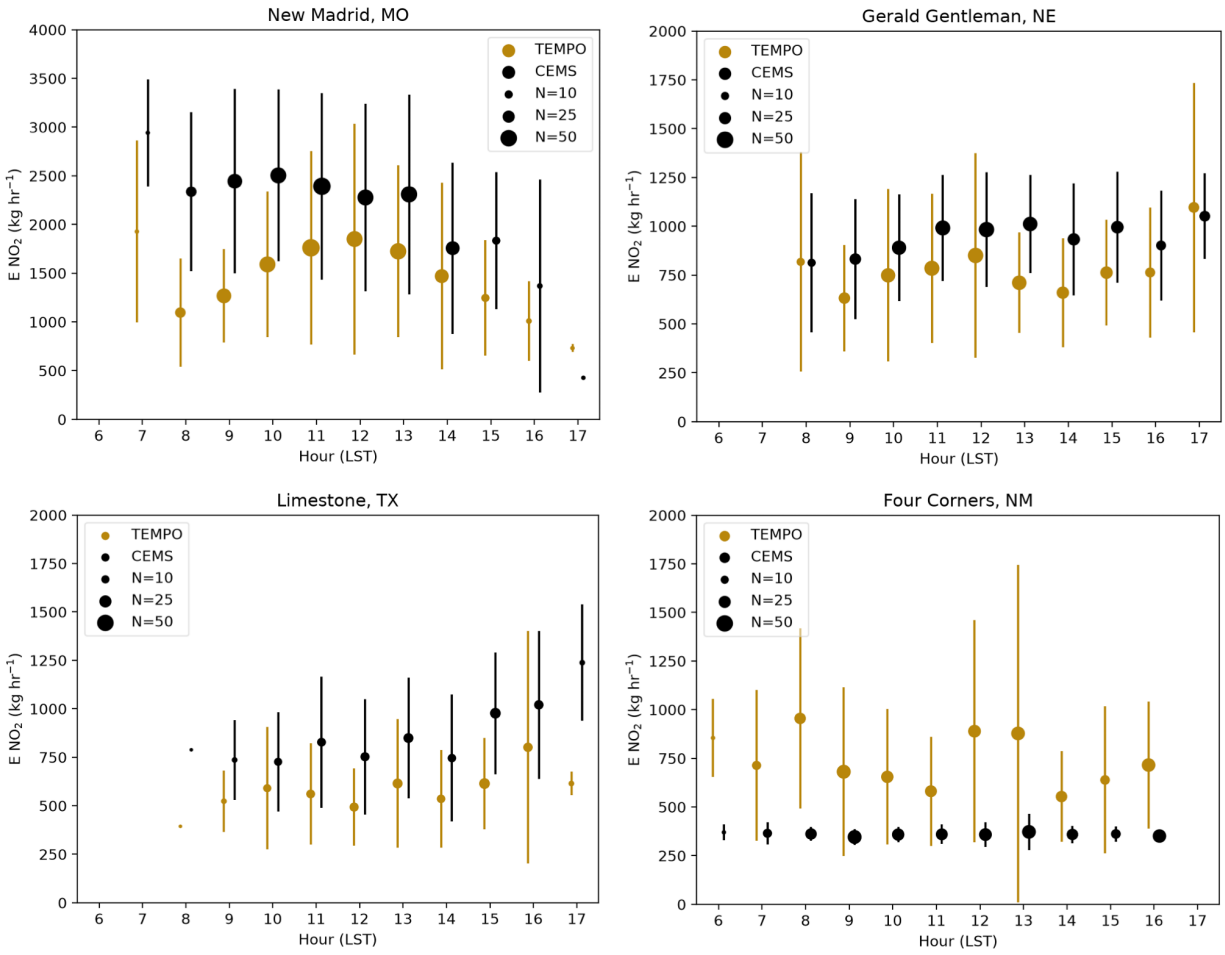

Figure S7: Similar to Figure 4(a) in the main text. Mean RD-derived TEMPO (light brown) and CEMS (black) emissions at 4 individual plants. Emissions are grouped by local hour, with the circle at the mean value and error bars showing standard deviation. Note that the top left plant, New Madrid, MO, has a different y-scale than the other three plants.

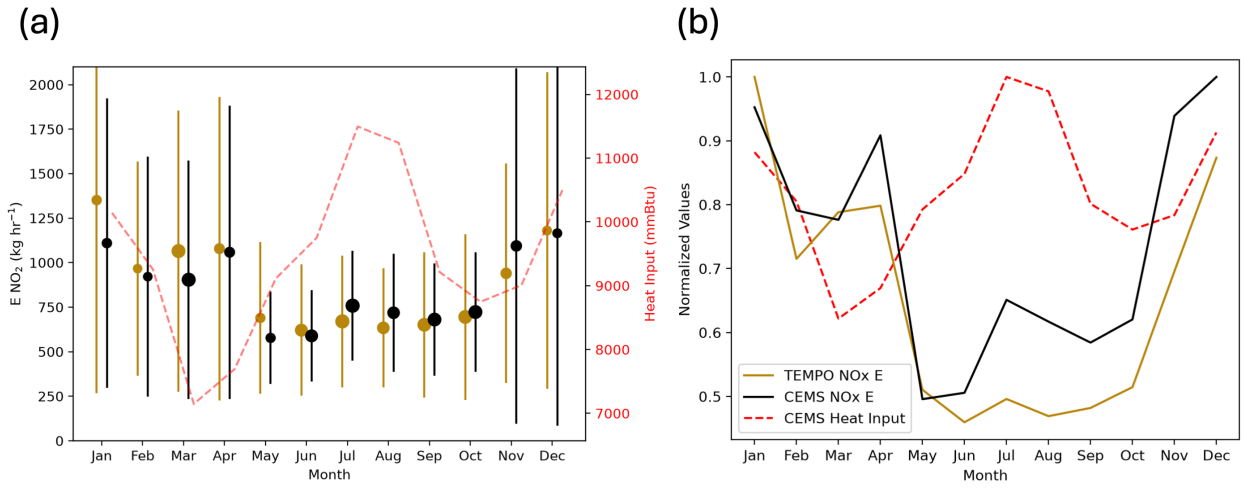

Figure S8: (a) Same as Figure 4(b) in main text, but with the mean heat input per hour in the CEMS inventory as a proxy for electrical generation. (b) Normalized seasonal profiles of the mean TEMPO-derived NO_x emissions, CEMS reported NO_x emissions, and CEMS reported heat input.

ORIS ID	Facility Name	State	Latitude	Longitude	Time Zone	UTC Offset	NRD Fits	NRD Fits w CEMS
2167	New Madrid Power Plant	MO	36.5147	-89.5617	America/Chicago	-6	333	309
298	Limestone	TX	31.4219	-96.2525	America/Chicago	-6	142	104
2168	Thomas Hill Energy Center	MO	39.5531	-92.6392	America/Chicago	-6	173	160
6076	Colstrip	MT	45.8831	-106.614	America/Denver	-7	283	280
6146	Martin Lake	TX	32.2597	-94.5703	America/Chicago	-6	158	157
6113	Gibson	IN	38.3722	-87.7661	America/Chicago	-6	79	53
6077	Gerald Gentleman Station	NE	41.0808	-101.1408	America/Chicago	-6	284	281
1001	Cayuga	IN	39.9239	-87.4272	America/Indiana/Indianapolis	-5	61	61
6204	Laramie River	WY	42.1103	-104.8828	America/Denver	-7	176	169
6481	Intermountain	UT	39.5035	-112.5811	America/Denver	-7	98	81
6641	Independence	AR	35.6733	-91.4083	America/Chicago	-6	118	117
4158	Dave Johnston	WY	42.8378	-105.7769	America/Denver	-7	253	240
1379	Shawnee	KY	37.1517	-88.775	America/Chicago	-6	124	122
3944	Harrison Power Station	WV	39.3844	-80.3325	America/New_York	-5	31	28
6139	Welsh Power Plant	TX	33.0583	-94.844	America/Chicago	-6	87	84
3935	John E Amos	WV	38.4731	-81.8233	America/New_York	-5	15	15
6068	Jeffrey Energy Center	KS	39.2825	-96.1153	America/Chicago	-6	114	112
6664	Louisa	IA	41.3153	-91.0936	America/Chicago	-6	110	108
994	IPL - Petersburg Generating Station	IN	38.5267	-87.2525	America/Indiana/Petersburg	-5	40	35
130	Cross	SC	33.3692	-80.1119	America/New_York	-5	21	20
6021	Craig	CO	40.4627	-107.5912	America/Denver	-7	21	21
7790	Bonanza	UT	40.0864	-109.2844	America/Denver	-7	66	60
8223	Springerville Generating Station	AZ	34.3186	-109.1636	America/Phoenix	-7	97	90
3490	Graham	TX	33.135	-98.6117	America/Chicago	-6	23	23
6101	Wyodak	WY	44.2886	-105.3847	America/Denver	-7	214	208
8066	Jim Bridger	WY	41.7378	-108.7875	America/Denver	-7	96	91
6190	Brame Energy Center	LA	31.395	-92.7167	America/Chicago	-6	8	7
1893	Boswell Energy Center	MN	47.2603	-93.6531	America/Chicago	-6	8	5
6194	Tolk Station	TX	34.1847	-102.5686	America/Chicago	-6	168	161
2442	Four Corners Steam Elec Station	NM	36.69	-108.4814	America/Denver	-7	303	300
6017	Newton	IL	38.9361	-88.2778	America/Chicago	-6	17	17
6178	Coleto Creek	TX	28.7128	-97.2142	America/Chicago	-6	8	7
7213	Clover Power Station	VA	36.8692	-78.7046	America/New_York	-5	8	6
6249	Winyah	SC	33.3303	-79.3611	America/New_York	-5	15	15
4162	Naughton	WY	41.7572	-110.5986	America/Denver	-7	43	43
6823	D B Wilson	KY	37.4497	-87.0803	America/Chicago	-6	32	28
6095	Sooner	OK	36.4537	-97.0527	America/Chicago	-6	61	58
8224	North Valmy	NV	40.8831	-117.1542	America/Los_Angeles	-8	45	45
3954	Mount Storm Power Station	WV	39.2014	-79.2667	America/New_York	-5	10	0
6213	Merom	IN	39.0694	-87.5108	America/Indiana/Indianapolis	-5	14	13
55076	Red Hills Generation Facility	MS	33.3761	-89.2183	America/Chicago	-6	10	9
6772	Hugo	OK	34.0158	-95.3206	America/Chicago	-6	9	9
3149	Montour, LLC	PA	41.0714	-76.6672	America/New_York	-5	8	7
160	Apache Station	AZ	32.0619	-109.8931	America/Phoenix	-7	50	49

2454	Cunningham	NM	32.7131	-103.3533	America/Denver	-7	123	123
50900	WestRock Virginia Corp Covington Ops	VA	37.7997	-79.9946	America/New_York	-5	25	24
6177	Coronado Generating Station	AZ	34.5778	-109.2717	America/Phoenix	-7	35	34
1353	Big Sandy	KY	38.1707	-82.6176	America/New_York	-5	6	5
6098	Big Stone	SD	45.3047	-96.5103	America/Chicago	-6	8	8
1004	Edwardsport Generating Station	IN	38.8067	-87.2472	America/Indiana/Vincennes	-5	12	12
8054	Gerald Andrus	MS	33.3503	-91.1181	America/Chicago	-6	27	9
7210	Cope Station	SC	33.3642	-81.03	America/New_York	-5	2	2
50835	TES Filer City Station	MI	44.217	-86.2906	America/Detroit	-5	0	0
6254	Ottumwa	IA	41.0961	-92.5556	America/Chicago	-6	9	7
10	Greene County	AL	32.6017	-87.7811	America/Chicago	-6	1	0
3478	Wilkes Power Plant	TX	32.8486	-94.5469	America/Chicago	-6	13	2
60	Gerald Whelan Energy Center	NE	40.5806	-98.3106	America/Chicago	-6	30	27
6004	Pleasants Power Station	WV	39.3668	-81.2944	America/New_York	-5	4	0
3504	Stryker Creek	TX	31.9381	-94.9883	America/Chicago	-6	0	0
10671	River Valley	OK	35.1931	-94.6458	America/Chicago	-6	4	2
56808	Virginia City Hybrid Energy Center	VA	36.9161	-82.3381	America/New_York	-5	3	0
55501	Tenaska Kiamichi Generating Station	OK	34.6831	-95.9349	America/Chicago	-6	10	7
4271	J P Madgett	WI	44.3026	-91.9126	America/Chicago	-6	1	1
525	Hayden	CO	40.4856	-107.185	America/Denver	-7	2	1
55380	Union Power Station	AR	33.2961	-92.5933	America/Chicago	-6	1	1
1396	Coughlin Power Station	LA	30.8442	-92.2606	America/Chicago	-6	0	0
113	Cholla	AZ	34.9394	-110.3033	America/Phoenix	-7	58	33